# Simultaneous recovery of origin time, hypocentre location and seismic moment tensor using sparse representation theory

Ismael Vera Rodriguez,[1,2] Mauricio Sacchi[1,2] and Yu J. Gu[1]

[1]*Physics Department, University of Alberta,* 4-183 *CCIS, Edmonton,* AB, T6G 2E1*, Canada. E-mail: verarodr@ualberta.ca*
[2]*Signal Analysis and Imaging Group (SAIG),* 4-183 *CCIS, Edmonton,* AB, T6G 2E1*, Canada*

**SUMMARY**
Using a proper parametrization, the source displacement field of a seismic event can be efficiently reconstructed by a redundant dictionary of Green's functions based on sparse representation theory. Then, by subjecting the pre-existing event records and pre-computed dictionary of Green's functions into a sparsity-promoting algorithm, it is possible to simultaneously evaluate the origin time, hypocentre coordinates and seismic moment tensor. The proposed method is applicable to single- or multiple-source scenarios and, with minor adjustments, can be a valuable tool for real-time, automatic monitoring systems. This study demonstrates the effectiveness and accuracy of the dictionary-based approach via (1) detection of microseismic events produced during the hydraulic fracturing of oil and gas wells and (2) inversion of a small-magnitude, regional earthquake (2002 June 18 in Caborn, Indiana) data. Our experiments based on numerical simulations and earthquake observations underscore the largely untapped potential of dictionary-based approaches and sparse representation theory in continuous source parameter recovery.

**Key words:** Inverse theory; Computational seismology; Early warning.

GJI Seismology

## 1 INTRODUCTION

The recovery of origin time, hypocentre location and moment tensor of seismic events is an inverse problem that has been widely investigated in the study of earthquakes. On a global scale, fast moment tensor inversions are routinely performed by institutions like the Global Centroid Moment Tensor (Global CMT) project (Dziewonski *et al.* 1981), the United States Geological Survey (USGS, Sipkin 1982) and the Earthquake Research Institute (ERI, Kawakatsu 1995). The CMT algorithm is mainly based on the pioneering work of Dziewonski *et al.* (1981), which expresses the source displacement field as a linear combination of 'excitation kernels'. These kernels are subsequently modified through perturbations to an initial source model to minimize a misfit function. This approach was later implemented by Kawakatsu (1995) for the analysis of long-period body-wave data archived at the ERI in Japan. Sipkin (1982) proposed two alternative methodologies, the first of which was based on the theory of optimal filter design. Under this approach, the seismic moment tensor is treated as a filter that produces the recorded displacement field through convolution with a set of Green's functions. Using least-squares techniques, this method determines the optimum values for the source mechanism. The second methodology is a non-linear approach that seeks a set of filters to convolve with the observed seismograms and produces

average values for each of the moment tensor elements. In all of the aforementioned methodologies, information about location and origin time is provided by an independent source and is required to initialize the inversion process.

At regional distances, fast solutions are also determined close to seismologically active zones. For example, in Northern and Central California, the Berkeley Seismological Laboratory operates two different systems for automatic determination of source mechanisms. The first is a time-domain method based on the non-linear relationship between the double couple (DC) source model and the source displacement field (Dreger & Helmberger 1993). The second is a frequency-domain approach designed to operate over surface wave data (Romanowicz 1982; Romanowicz *et al.* 1993). These two methods have been automated (Pasyanos *et al.* 1996) and the time-domain approach has been integrated into the TDMT_INV distributable package (Dreger 2003); the latter is currently used for moment tensor inversions by several institutions around the world (e.g. Dreger 2003; Clinton *et al.* 2006; Scognamiglio *et al.* 2009). Bernardi *et al.* (2004) present a feasibility analysis of a system for automatic, near real-time source parameters recovery in the European–Mediterranean region. Similar to methods used for global monitoring, the aforementioned regional inversion routines are triggered only when pre-existing information about earthquake occurrence is available. For instance, a lag time for the calculation

of the information necessary to start the estimation of the source moment tensor is implicitly required in all of these monitoring systems. The feasibility of a continuous, automatic, real-time source parameter (origin time, hypocentre location and moment tensor) monitoring system is examined by Tajima *et al.* (2002). The system is based on the grid search algorithm (Kawakatsu 1998) currently adopted for the monitoring of earthquakes in California (Guilhem & Dreger 2010) and Japan (Tsuruoka *et al.* 2009). Also, the grid search method using 3-D Green's functions has been tested to monitor seismic activity in Taiwan (Lee *et al.* 2010). The main difference of the grid search approach from other monitoring systems, aside from not requiring *a priori* information, is its capability to operate over a continuous flow of seismic data. On the other hand, being a grid-based approach, is limited by a maximum number of gridpoints and station recordings that can be handled without compromising real-time response.

Besides earthquake monitoring, fast estimations of the source parameters can have an important impact on applied geophysics, particularly the study of microseismic sources induced by hydraulic fracturing of oil and gas wells. Oil and gas wells are fractured to enhance production (Cipolla & Wright 2002). This is achieved through the injection of fluids at high pressures, which percolate into rock formations and potentially trigger microseismic events that are recorded in nearby receiver locations (Maxwell 2005; Duncan & Eisner 2010; Maxwell *et al.* 2010). By analysing the properties of the induced seismicity, interpreters generate estimates of fracture's geometry, complexity, permeability and connectivity with pre-existing faults and/or fractures (e.g. House *et al.* 1996; Shapiro *et al.* 1999; Maxwell *et al.* 2002; Rothert & Shapiro 2007; Fischer *et al.* 2008; Bayuk *et al.* 2009; Warpinski 2009). A thorough understanding of the fractures induced through hydraulic injection is important for the planning and development of an oilfield (Cipolla & Wright 2002). The source mechanism of microseismic events can provide information to elaborate models of fracture propagation (Warpinski 1994; Warpinski *et al.* 2001), to study the state of stresses in the neighbourhood of the injection well (House *et al.* 1996; Rutledge & Phillips 2003) and, in general, as a source of information to analyse the effectiveness of the induced fractures. The importance in obtaining information about fracture propagation during the injection process has been largely recognized (Maxwell *et al.* 2002; LeCampion & Jeffrey 2004; Le Calvez *et al.* 2006); however, the estimation of source mechanisms is still usually performed in a post-processing stage. Additionally, methodologies used for inversion of moment tensors with microseismic data do not produce simultaneous estimates of the three source parameters (e.g. Nolen-Hoeksema & Ruff 2001; Rutledge & Phillips 2003; Jechumtalova & Eisner 2008; Sileny *et al.* 2009; Godano *et al.* 2010). Hypocentre locations and origin times are estimated independently, which introduces a lag time for the purpose of real-time implementation. Fast availability of source geometries is a valuable tool that can be incorporated into the decision-making process during a hydraulic injection.

In this study we present a method for the simultaneous recovery of the three source parameters (origin time, hypocentre location and seismic moment tensor). This 'waveform fitting' method is a modification of the Block Orthogonal Matching Pursuit (BOMP) from sparse representation theory (Eldar *et al.* 2010). In the standard BOMP methodology, the global maximum in the $\ell_2$-norm function of the correlation between the blocks of the dictionary and the current residual is selected as the index of a new block that participates in the representation of the input signal. With a modification proposed in this work, the misfit for solutions in the $n_h$ positions with the largest $\ell_2$-norm function are computed, and the position of the new block in the representation of the signal is selected where the misfit is minimum. This modification permits the recovery of optimal solutions in highly coherent dictionaries, which we will see is the most common scenario for seismic source monitoring applications. Advantages of the proposed method with respect to others include: no *a priori* information about event occurrence is required; potential for continuous, automatic, real-time performance; multiple simultaneous sources can be inverted from the same set of observations; and its suitability to perform in a particular scale of application is controlled by the availability of appropriate Green's functions to 'match' the observations. In comparison, the inversion method proposed here provides similar capabilities and fewer limitations than the grid search algorithm from Kawakatsu (1998), in other words, where the grid search approach can perform in real time our method can also do. However, the most important relevance of the methodology presented here is that it can be used in conjunction with 'compressive sensing' (Donoho *et al.* 2006; Baraniuk 2007; Candes & Wakin 2008) to increase the number of grid nodes that can be inverted in real time, allowing also the use of a significantly larger number of input recordings to the inversion system (Vera Rodriguez *et al.*, 2010b).

The manuscript is organized as follows. In Section 2 a review on important definitions from sparse representation theory is presented and this section is complemented with the forward parametrization of the source parameter inversion. Section 3 presents our two main contributions: the link between the source parameter inversion and sparse representation theory, and a methodology for the recovery of the source parameters based on BOMP. Section 4 presents applications of the proposed methodology to both synthetic and real cases. The synthetic case corresponds to the setting of a microseismic monitoring experiment. The real data set is an earthquake scenario using records from the 2002 June 18 Caborn Indiana earthquake. Finally, Sections 5 and 6 are devoted to the discussion and conclusions from this study.

## 2 THEORETICAL BACKGROUND

### 2.1 Block sparsity

We start our discussion by introducing some definitions from sparse representation theory that apply to general signals. The description that follows is rather general, hence the reader is referred to the articles cited within the text to find further details on the definitions introduced in this section. Later in Section 3, the connection between this general theory and the problem of our interest is presented. Suppose a discrete signal $\mathbf{y} \in \mathbb{R}^L$ is a linear combination of a subset of the functions $\boldsymbol{\psi}_j \in \mathbb{R}^L$, $j = 1, 2, \ldots, N$, that is,

$$\mathbf{y} = \boldsymbol{\Psi}\mathbf{x}, \tag{1}$$

where $\boldsymbol{\Psi} = [\boldsymbol{\psi}_1, \boldsymbol{\psi}_2, \ldots, \boldsymbol{\psi}_N] \in \mathbb{R}^{L \times N}$, and $\mathbf{x} \in \mathbb{R}^N$ is a vector containing the coefficients representing the signal. By this definition, a coefficient $x_j$ with zero value corresponds to a function $\boldsymbol{\psi}_j$ that does not participate in the representation of $\mathbf{y}$. Vector $\mathbf{x}$ is said to be *S*-sparse (Baraniuk 2007; Candes & Wakin 2008) if $||\mathbf{x}||_0 \leq S \ll N$, where the symbol $|| \cdot ||_0$ refers to the $\ell_0$-norm of the variable between vertical bars. The $\ell_0$-norm is defined as the count of the non-zero elements in the variable under consideration

(e.g. if $\mathbf{x} = [1,0,3,0,0,-5,0,4]$, then $||\mathbf{x}||_0 = 4$) (Mallat 2008). In the signal processing community, matrix $\mathbf{\Psi}$ and its columns are generally referred to as dictionary and atoms, respectively (Mallat & Zhang 1993). The dictionary is overcomplete or redundant if $L < N$, which also corresponds to an underdetermined system of equations (Mallat 2008). A vector $\mathbf{x}$ is said to display 'block sparsity' if its non-zero coefficients occur in clusters (Eldar & Bolcskei 2009). Under this consideration, the vector $\mathbf{x}$ can be expressed as a concatenation of blocks,

$$\mathbf{x} = [\,\mathbf{x}[1] \quad \mathbf{x}[2] \quad \cdots \quad \mathbf{x}[N_t]\,]^T, \tag{2}$$

where $\mathbf{x}[l] = [x_{d(l-1)+1}, x_{d(l-1)+2}, \cdots, x_{d(l-1)+d}]$ is the $l$th block and $N_t$ is the total of blocks in $\mathbf{x}$. The length of each block is $d$, such that $N = N_t d$. Correspondingly, the dictionary $\mathbf{\Psi}$ is the concatenation of the column blocks

$$\mathbf{\Psi} = [\,\mathbf{\Psi}[1] \quad \mathbf{\Psi}[2] \quad \cdots \quad \mathbf{\Psi}[N_t]\,], \tag{3}$$

where $\mathbf{\Psi}[l] = [\boldsymbol{\psi}_{d(l-1)+1}, \boldsymbol{\psi}_{d(l-1)+2}, \cdots, \boldsymbol{\psi}_{d(l-1)+d}]$ is the $l$th column block. The vector $\mathbf{x}$ is said to be block $K$-sparse if $||\mathbf{x}||_{2,0} \leq K \ll N_t$, where $||\cdot||_{2,0}$ denotes the mixed $\ell_{2,0}$-norm (Kowalski & Torrésani 2009; Eldar *et al.* 2010) that counts the number of blocks with non-zero $\ell_2$-norm. In sparse representation theory, an important property that characterizes a dictionary is the measurement of how alike are its atoms. A common metric to determine the similarity between the atoms of a dictionary is called mutual coherence (e.g. Tropp 2004). In the case of block sparsity, two different measurements of coherence can be defined, one is the coherence within a block or subcoherence and the second is the coherence between different blocks. The subcoherence $\nu$ is computed as (Eldar *et al.* 2010, eq. 8)

$$\nu = \max_l \left( \max_{i,j \neq i} \left| \boldsymbol{\psi}_i^T \boldsymbol{\psi}_j \right| \right), \quad \boldsymbol{\psi}_i, \boldsymbol{\psi}_j \in \mathbf{\Psi}[l]. \tag{4}$$

On the other hand, the block coherence is defined as (Eldar *et al.* 2010, eq. 6)

$$\mu_B = \max_{l, r \neq l} \left[ \frac{1}{d} \rho(\mathbf{M}[l,r]) \right], \tag{5}$$

where $\rho(\cdot)$ is the spectral norm (Strang 2006) of the matrix $\mathbf{M}[l,r]$ given by

$$\mathbf{M}[l,r] = \mathbf{\Psi}^T[l]\mathbf{\Psi}[r]. \tag{6}$$

## 2.2 Recovery of block $K$-sparse solutions

The recovery of a block $K$-sparse solution $\mathbf{x}$ from a set of observations $\mathbf{y}$ is accomplished through modifications to Basis Pursuit (BP, Chen *et al.* 1998) and Orthogonal Matching Pursuit (OMP, Pati *et al.* 1993) algorithms. We further propose a source parameter inversion method based on BOMP (Eldar *et al.* 2010). BOMP is a greedy algorithm that works iteratively selecting one by one the blocks of the dictionary that participate in the representation of the signal. Using least-squares criteria, BOMP selects after each iteration the block of the dictionary that provides the best improvement in quality for the signal representation. The details of BOMP are as follows:

---

**Algorithm 1.** BOMP

**1. Initialize variables**
residual $\mathbf{r}_0 = \mathbf{y}$
index set $\mathbf{\Lambda}_0 = \emptyset$
counter $l = 1$

**2. Identify the block that best matches the current residual**
$n_l = \arg\max_n ||\mathbf{\Psi}^T[n]\mathbf{r}_{l-1}||_2^2$
$\mathbf{\Lambda}_l = \mathbf{\Lambda}_{l-1} \cup n_l$

**3. Estimate the best approximation coefficients with the blocks chosen so far**
$\{\mathbf{x}_l[n]\}_{n \in \mathbf{\Lambda}_l} = \arg\min_{\{\mathbf{a}[n]\}_{n \in \mathbf{\Lambda}_l}} ||\mathbf{y} - \sum_{n \in \mathbf{\Lambda}_l} \mathbf{\Psi}[n]\mathbf{a}[n]||_2^2$

**4. Update the residual and iterate**
$\mathbf{r}_l = \mathbf{y} - \sum_{n \in \mathbf{\Lambda}_l} \mathbf{\Psi}[n]\mathbf{x}_l[n]$
$l = l + 1$

repeat 2 - 4 until the stopping criteria are met.

**5. Ouput**
solution vector $\mathbf{x}[n] = \mathbf{x}_l[n]$ for $n \in \mathbf{\Lambda}_l$ and $\mathbf{x}[n] = 0$ otherwise.

---

Using BOMP and considering a model as in eq. (1), a block $K$-sparse representation $\mathbf{x}$ is uniquely recovered if (Eldar *et al.* 2010, theorem 3),

$$Kd < \frac{1}{2}\left(\frac{1}{\mu_B} + d - (d-1)\frac{\nu}{\mu_B}\right). \tag{7}$$

In these cases, the algorithm stops when the updated residual is zero. In practical situations, however, we have models of the following form:

$$\hat{\mathbf{y}} = (\mathbf{\Psi} + \hat{\mathbf{\Psi}})\mathbf{x} + \mathbf{n}, \tag{8}$$

where $\hat{\mathbf{\Psi}}$ is a perturbation to the dictionary, $\mathbf{n}$ is additive noise and $\hat{\mathbf{y}}$ is a set of inaccurate observations. Under the more realistic model (8), one way to proceed is to look for an optimal block $K$-sparse approximation, that is, the solution to

$$\min_{||\mathbf{x}||_{2,0}=K} \quad \min_{\mathbf{x}} ||\hat{\mathbf{y}} - (\mathbf{\Psi} + \hat{\mathbf{\Psi}})\mathbf{x}||_2^2. \tag{9}$$

In these cases, BOMP must be provided with a stopping criteria after $K$ iterations. In practical scenarios, we always look for having dictionaries where the perturbation $\hat{\mathbf{\Psi}}$ is small. If $\hat{\mathbf{\Psi}}$ is negligible, Donoho *et al.* (2006) show that the error in the estimation of $\mathbf{y}$ depends directly on the level of noise $\mathbf{n}$, and furthermore, that the optimal approximation $\hat{\mathbf{x}}$ shares the same support as the sparse representation $\mathbf{x}$ of the noiseless signal. If $\hat{\mathbf{\Psi}}$ is not negligible, Herman & Strohmer (2010) demonstrate both theoretically and numerically that the error in the estimation of $\mathbf{y}$ increases linearly with the amount of perturbation introduced to the dictionary but anticorrelate with the sparsity of $\mathbf{x}$. Up to this point, we have described results from sparse representation theory that apply to general signals. After introducing the source parameter inversion problem in the following subsection, the connection between sparse representations and the seismic source monitoring problem will become clear.

## 2.3 Displacement field due to a seismic source

The far displacement field due to a point source is estimated using the expression (Aki & Richards 2009, eq. 3.23)

$$u_n(\mathbf{x}, t) = M_{pq}(t) * \frac{\partial}{\partial \xi_q} G_{np}(\mathbf{x}, t; \boldsymbol{\xi}, 0), \tag{10}$$

where **x** is the position of the recording station and $\boldsymbol{\xi}$ is the source location. The term $M_{pq}(t)$ is the moment tensor of the seismic source and $G_{np}$ are 'the point force' Green's functions containing information about the wave propagation between **x** and $\boldsymbol{\xi}$. The subscript $n$ is related to the ground motion component and the symbol $*$ denotes convolution. Expression (10) holds for any type of media with the appropriate use of Green's functions. Assuming that the source geometry can be separated from its time variation (Madariaga 2007), we can write

$$u_n(\mathbf{x}, t) = M_{pq} g_{np,q}(\mathbf{x}, t; \boldsymbol{\xi}, 0). \tag{11}$$

In eq. (11), the seismic moment tensor has been split into a time invariant part $M_{pq}$ and a source time function $s(t)$, where $g_{np,q}(\mathbf{x}, t; \boldsymbol{\xi}, 0) = s(t) * \frac{\partial}{\partial \xi_q} G_{np}(\mathbf{x}, t; \boldsymbol{\xi}, 0)$. Arranging terms in matrix form, eq. (11) can also be expressed as

$$\mathbf{u} = \mathbf{Gm}, \tag{12}$$

where **m** contains the six independent elements of the time invariant part of the moment tensor (from now on, the moment tensor) arranged in column vector form and the columns of matrix **G** are the functions $g_{np,q}$ (for short, the Green's functions). The formulation in (12) is developed for observations due to a single source recorded at multiple stations.

# 3 USING SPARSE REPRESENTATION THEORY TO INVERT FOR THE SOURCE PARAMETERS

The displacement field due to multiple sources can be expressed as

$$\mathbf{u} = \sum_s \mathbf{G}_s \mathbf{m}_s, \tag{13}$$

where the subscript $s$ refers to a particular source. One way to implement eq. (13) is by setting a grid over the space where seismic sources are expected to occur. Then, every node in the grid can be considered a potential source location or 'virtual source' (Kawakatsu 1998). Following this approach, eq. (13) can be simplified to

$$\mathbf{u} = \mathbf{Gm}. \tag{14}$$

In this case, the matrix **G** contains the six Green's functions for all node–station combinations, and vector **m** includes the moment tensors for all the virtual sources in the grid (Fig. 1), that is,

$$\mathbf{G} = [\, \mathbf{G}[1] \quad \mathbf{G}[2] \quad \cdots \quad \mathbf{G}[N_t] \,],$$

and

$$\mathbf{m} = [\, \mathbf{m}[1] \quad \mathbf{m}[2] \quad \cdots \quad \mathbf{m}[N_t] \,]^T,$$

where the block $\mathbf{m}[l] = [m_{11}^l, m_{12}^l, m_{13}^l, m_{22}^l, m_{23}^l, m_{33}^l]$ is the seismic moment tensor of the $l$th node (virtual source), $\mathbf{G}[l]$ the column block of the corresponding Green's functions, and $N_t$ is the total number of grid nodes. For a grid of $N_t = N_x \times N_y \times N_z$ nodes, the size of **G** is $(L \times N)$, where $N = 6 \times N_t$ and $L$ = number of receivers × number of receiver's components × number of samples in one component trace. For a given time period, the blocks with non-zero $\ell_2$-norm in the vector **m** are those corresponding to the node locations where seismic sources have actually taken place. If, for example, in a set of observations **u** we only have the displacement field due to one seismic source, then vector **m** is block 1-sparse ($\|\mathbf{m}\|_{2,0} = 1 \ll N_t$). Therefore, the connection between the block sparse representation problem and (14) is straightforward. The matrix $\mathbf{G} \in \mathbb{R}^{L \times N}$ is a dictionary of Green's functions, while vector
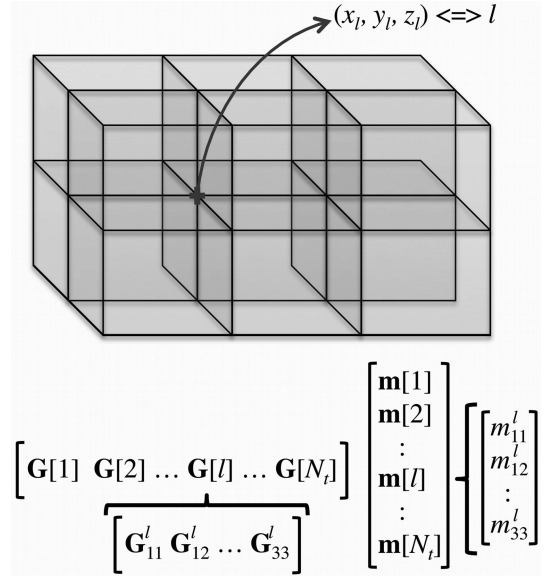
**Figure 1.** Mapping between the subsurface grid volume and the dictionary of Green's functions. Every node in the grid has spatial coordinates $(x, y, z)$ and a linear index $l \in [1, N_t]$ where $N_t$ is the total of nodes in the grid. Hence, the spatial coordinates of the $l$th node are $(x_l, y_l, z_l)$. A set of six Green's functions corresponding to each of the independent elements of the seismic moment tensor are computed at each grid node. Every set of Green's functions form a block of the dictionary of Green's functions **G** in eq. (14). Correspondingly, every block in the solution vector **m** is associated to a location in the subsurface grid volume. Hence, the blocks in **m** with $\ell_2$-norm different from zero provide the location and moment tensor coefficients where sources in the grid have taken place. An extension in time of the dictionary provides also the origin times of the sources.

$\mathbf{m} \in \mathbb{R}^N$ is a block sparse representation of the source displacement field under that dictionary. By identifying the blocks $\mathbf{m}[l]$, with $d = 6$, that have $\ell_2$-norm different from zero, we are in fact determining the source mechanisms (magnitudes of the elements in each block $\mathbf{m}[l]$), the hypocentre coordinates (corresponding to the locations of the Green's functions that expand the blocks $\mathbf{m}[l]$) and the origin times (given by the times where the blocks $\mathbf{m}[l]$ are found) of the seismic events represented in **u**. An algorithm to accomplish such purpose is proposed in the following section.

## 3.1 Algorithm to invert for the source parameters based on a block sparse representation

The proposed methodology is a BOMP algorithm applied over an augmented dictionary of Green's functions. Hence, using the augmented dictionary, a set of Green's functions and a vector of observations are compared across a 3-D volume and time to estimate optimal parameters for origin time and location of seismic events. The augmented dictionary of Green's functions is defined as

$$\mathbb{G} = [\, \mathbf{G}_0 \quad \mathbf{G}_1 \quad \mathbf{G}_2 \quad \ldots \quad \mathbf{G}_{N_w-1} \,], \tag{15}$$

where $\mathbf{G}_k$ is the dictionary of Green's functions for the whole grid delayed in time by $k$ samples. Note that $\mathbf{G}_0$ is basically the same as **G** from eq. (14) (for the rest of the exposition, the variable **G** will refer to that of eq. 14 unless otherwise stated). To simplify the presentation the augmented dictionary $\mathbb{G}$ will be called superdictionary and the delayed dictionaries $\mathbf{G}_k$ superblocks. Hence a superblock $\mathbf{G}_k$ of $\mathbb{G}$ is a $k$ samples delayed version of the dictionary **G** whose column blocks are the sets of six Green's functions $\mathbf{G}[l]$ for each

node $l$ in the grid. The superdictionary $\mathbb{G}$ can be seen either as formed by the superblocks $\mathbf{G}_k$ specified by a single index $k$, or by the blocks $\mathbf{G}_k[l]$ specified by the two indices $(k, l)$. Considering its physical meaning, sometimes we will refer to the block index $l$ as a position index and to the index $k$ as a delay index (which is related to the origin time). The maximum delay $N_w - 1$ is determined by the processing window selected by the user as we will show in the following paragraphs.

Consider a network of $N_{st}$ three-component seismic stations transmitting a continuous flow of seismic recordings to a computing centre. At the computing centre the recordings are cut in windows of duration $t_{N_u}$. If we consider a sampling rate of $\Delta t$ this results in sets of $3 \times N_{st}$ traces of $N_u = t_{N_u}/\Delta t$ samples. The subsurface volume of interest is divided using a grid as established before. Then, Green's functions at each grid node are computed and stored to form a dictionary $\mathbf{G}$. The time duration of a Green's function is $t_{N_G}$, where $t_{N_G}$ is determined by the longest arrival time for the wave phases of interest between all possible combinations of grid nodes and seismic stations. The number of samples in a Green's function is $N_G = t_{N_G}/\Delta t$. The row size of the dictionary of Green's functions $\mathbf{G}$ is $L = 3 \times N_{st} \times N_G$. The length of a Green's function is related to the length of the observations by $N_u = N_G + N_w$. To compute the superdictionary $\mathbb{G}$, the dictionary $\mathbf{G}$ is delayed and padded with zeros to create $N_w$ superblocks $\mathbf{G}_k$ with row length $N_u$. An efficient implementation of this methodology does not require to create the delayed dictionaries $\mathbf{G}_k$. Instead, the input observation traces are successively cut to the length of the original Green's functions $N_G$ simulating the required time delays. In fact, the concept of super-dictionary and superblocks is only used here as a means to simplify the presentation. The steps followed by BOMP for the recovery of the source parameters can be summarized as follows

### Step 1. Initialization of variables

The observations are arranged in a column vector $\mathbf{u}$ and a residual $\mathbf{r}_0 = \mathbf{u}$ is initialized. Also, the index sets $\Lambda_0$ and $\Gamma_0$ are initialized as empty, and the iteration counter $i$ is set to 1.

### Step 2. Identification of the best origin time and source location

For each superblock $\mathbf{G}_k[l]$, the function $f(k, l) = ||\mathbf{G}_k^T[l]\mathbf{r}_{i-1}||_2^2$ is computed for all the column blocks $l \in [1, N_t]$ and delays $k \in [0, N_w - 1]$. For the next step, we identify the delay index $k$ (origin time), and position index $l$ that corresponds to the global maximum in the function $f(k, l)$. In other words, we find the indices

$$n_i = \arg\max_k [f(k, l)], \quad k \in [0, N_w - 1], \quad l \in [1, N_t],$$

$$m_i = \arg\max_l [f(k, l)], \quad k \in [0, N_w - 1], \quad l \in [1, N_t].$$

The identified origin time and source location indices are then saved with those found in previous iterations,

$$\Gamma_i = \Gamma_{i-1} \cup n_i,$$

$$\Lambda_i = \Lambda_{i-1} \cup m_i.$$

After step 2 of the $i$th iteration, each of the sets $\Gamma_i$ and $\Lambda_i$ contain a total of $i$ indices. Step 2 is the most time consuming part of the method.

### Step 3. Updating of the source mechanisms

The source mechanisms for all identified sources are updated. For such objective, a matrix $\mathbf{A}_i$ is formed with the Green's function blocks specified by the index sets $\Gamma_i$ and $\Lambda_i$. These Green's functions correspond only to the locations and origin times of the sources identified in the previous step, hence, the matrix $\mathbf{A}_i$ has a much smaller number of columns than matrix $\mathbb{G}$. The matrix $\mathbf{A}_i$ is defined as (for $i > 2$)

$$\mathbf{A}_i = \begin{bmatrix} \mathbf{G}_{\Gamma_i[1]}[\Lambda_i[1]] & \mathbf{G}_{\Gamma_i[2]}[\Lambda_i[2]] & \dots & \mathbf{G}_{\Gamma_i[i]}[\Lambda_i[i]] \end{bmatrix}.$$

For $i = 1$ or 2, matrix $\mathbf{A}_i$ is formed by only the first one or two blocks, respectively. Then, the moment tensors from all sources so far identified are simultaneously updated,

$$\tilde{\mathbf{m}}_i = (\mathbf{A}_i^T \mathbf{A}_i)^{-1} \mathbf{A}_i^T \mathbf{u}.$$

In this step a constraint can also be imposed to the inversion. For example, the deviatoric constraint is linear and can be easily incorporated (Aki & Richards 2009).

### Step 4. Update the residual and iterate

The contributions to the displacement field corresponding to all the sources found up to the current iteration are subtracted from the original observations to generate a new residual vector,

$$\mathbf{r}_i = \mathbf{u} - \mathbf{A}_i \tilde{\mathbf{m}}_i.$$

Finally, the counter is updated to $i = i + 1$. Steps 2–4 are repeated until a stopping criteria is met. Every iteration of the code finds 1 seismic event.

### Step 5. Output

The output from the inversion code are the origin times given by the index set $\Gamma_i$, the hypocentre locations given by the index set $\Lambda_i$ and the updated moment tensors $\tilde{\mathbf{m}}_i$.

### 3.2 Proposed modification to the BOMP algorithm

Consider the ideal case with accurate Green's functions and no additive noise in the observations. If comparing the blocks $\mathbf{G}_k[l]$, the superdictionary $\mathbb{G}$ meets inequality (7), then BOMP will always find an optimum set of source parameters. In other words, the origin times, locations and source mechanisms that correspond to the sparsest representation of the displacement field in terms of $\mathbb{G}$. Origin time and location will also correspond to the correct source parameters for the actual seismic events, however, the correctness of the source mechanisms will depend on the conditioning and constraint applied to the inversion in step 3. In practical terms, inequality (7) states that the columns of the superdictionary $\mathbb{G}$ have to be sufficiently different to allow the algorithm to identify the correct set of Green's functions at each iteration. The subcoherence and coherence are the way to quantify how alike are the columns within a block, and between different blocks of $\mathbb{G}$, respectively. It is immediately obvious that the coherence between blocks corresponding to the same node $n_l$ at different time delays (e.g. $\mathbf{G}_{k_1}[n_l]$ and $\mathbf{G}_{k_2}[n_l]$, where $k_1 \neq k_2$) will in general have very high coherence. In this case, a possible alternative to reduce the coherence would be to increase the amount of time delay $k \cdot \Delta t$ between superblocks, however, this still does not guarantee compliance of inequality (7), while the resolution in origin time estimation would be negatively affected. The coherence between blocks of the same superblock $n_k$

(e.g. between $\mathbf{G}_{n_k}[l_1]$ and $\mathbf{G}_{n_k}[l_2]$, where $l_1 \neq l_2$) is influenced by the frequency content and distance between the grid nodes. For the same distance between nodes, the lower the frequency content, we expect the coherence between blocks to increase due to the overlapping of wave arrivals. Equivalently, fixing the frequency content, the coherence between blocks should increase if the distance between nodes is reduced. In a practical scenario, it is desirable to have combinations of node distance–frequency content where the wave arrivals between adjacent nodes overlap, otherwise, a considerable amount of error in the estimated moment tensors is introduced for seismic sources whose real location is not coincident with one of the grid nodes. The subcoherence within a block is always high, since energy arrivals are located at similar times in the six Green's functions forming the block. It has to be pointed out, however, that while meeting inequality (7) is a guarantee of success, not meeting it is not a guarantee of failure. In other words, inequality (7) is a guarantee of success in the worst case scenario (Eldar *et al.* 2010), which means that even if $\mathbb{G}$ does not comply with it, there will be multiple cases where BOMP will still be able to pick optimum solutions. The key to be in these scenarios, is to create a $\mathbb{G}$ where the chances of success are much higher than the chances of failure. Additionally, BOMP can also be modified to increase its chances of finding optimum solutions. Here, we introduce a modification that splits step 2 in Section 3.1 into different substeps, these are as follows:

### Step 2.1

Compute the function $f(k, l) = ||\mathbf{G}_k^T[l]\mathbf{r}_{i-1}||_2^2$ as presented before (Fig. 2a). Take the indices $(k, l)$ of the $n_h$ largest values in $f(k, l)$ and save them into a new variable $\mathbf{h}[p] = [k_p, l_p], p \in [1, n_h]$ (Fig. 2b). Then, moment tensor solutions at each index pair $\mathbf{h}[p]$ are calculated with

$$\tilde{\mathbf{s}}_{k_p}[l_p] = \left(\mathbf{G}_{k_p}^T[l_p]\mathbf{G}_{k_p}[l_p]\right)^{-1}\mathbf{G}_{k_p}^T[l_p]\mathbf{r}_{i-1}, \quad p \in [1, n_h].$$

If a constrained inversion is to be used, then it should also be considered at this substep.

### Step 2.2

For every solution $\tilde{\mathbf{s}}_{k_p}[l_p]$ a normalized misfit (NM) measure is estimated, this is

$$\mathrm{NM}_{k_p}[l_p] = \frac{||\mathbf{G}_{k_p}[l_p]\tilde{\mathbf{s}}_{k_p}[l_p] - \mathbf{r}_{i-1}||_2^2}{||\mathbf{r}_{i-1}||_2^2}, \quad p \in [1, n_h].$$

Finally, the indices $(k_p, l_p)$ corresponding to the solution $\tilde{\mathbf{s}}_{k_p}[l_p]$ that minimizes the $\mathrm{NM}_{k_p}[l_p]$ function are the ones saved in the index sets $\mathbf{\Gamma}$ and $\mathbf{\Lambda}$ (Fig. 2c). In general, $n_h \ll N_t$ to reduce the impact of this modification over the processing time. The search of minimum misfit solutions over the $\mathrm{NM}_{k_p}[l_p]$ function allows BOMP the determination of optimum solutions in highly coherent dictionaries, making it suitable for source parameter determination.

### 3.3 Stopping criteria

In practical scenarios, both BOMP and the modified BOMP have to be provided with a stopping criteria after $N_s$ iterations. Since the algorithms find the source parameters of a seismic event at every iteration, it is natural to set $N_s$ equal to the number of maximum expected sources in each input observations vector. For example, in
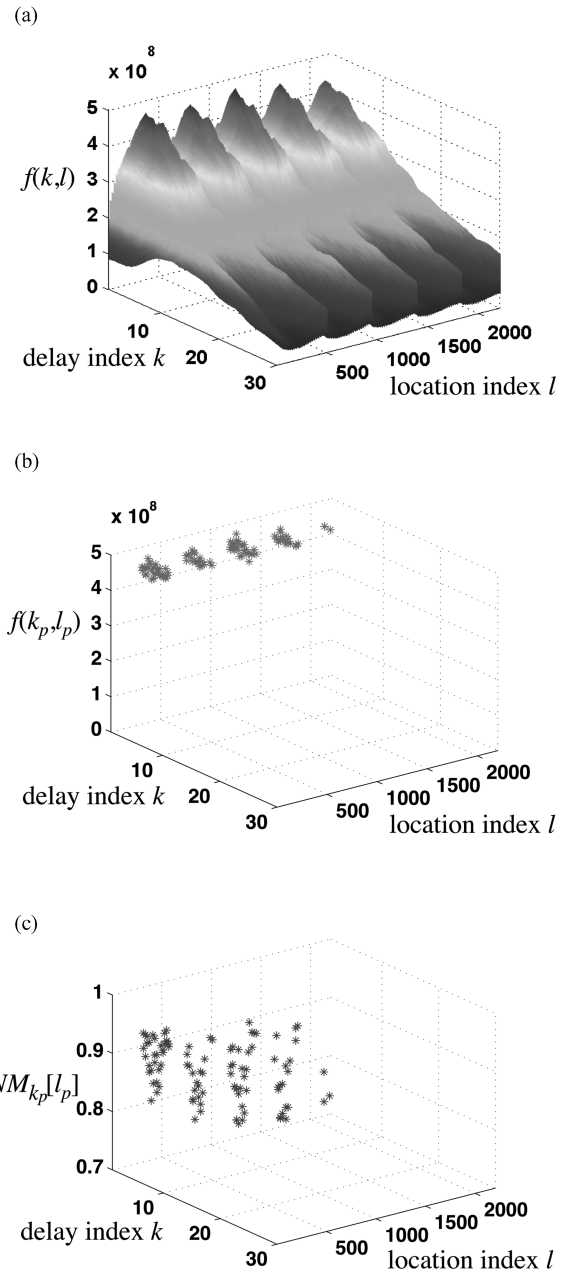
(a)

(b)

(c)

**Figure 2.** Real data example of the modification introduced to the BOMP algorithm. (a) Function $f(k, l) = ||\mathbf{G}_k^T[l]\mathbf{r}_0||_2^2$, the total number of nodes in the grid of this example is $N_t = 2205$, hence $l \in [1, 2205]$, the processing window is $N_w = 30$, hence $k \in [0, 29]$. (b) Plot of the $n_h$ largest values in (a), in this example $n_h = 100$, therefore $p \in [1, 100]$. (c) Normalized misfit for solutions computed at each $(k_p, l_p)$ indices that correspond to values of $f(k_p, l_p)$ displayed in (b). The delay index $k_p$ and position index $l_p$ where the NM is minimum are considered the optimum origin time and location for a seismic source, and therefore saved in the index sets $\mathbf{\Gamma}$ and $\mathbf{\Lambda}$. In the regular BOMP workflow the indices $(k, l)$ that correspond to the global maximum in (a) are taken as the optimum origin time and location of the seismic source.

an earthquake scenario a straightforward value is $N_s = 1$. However, the algorithms will always output a solution after $N_s$ iterations even if no seismic events are recorded in the observations at all. To discriminate between valid and spurious solutions, a detectability threshold $\alpha_d$ is implemented (Fig. 3). In each iteration $i$, a $\mathrm{NM}_i$ is
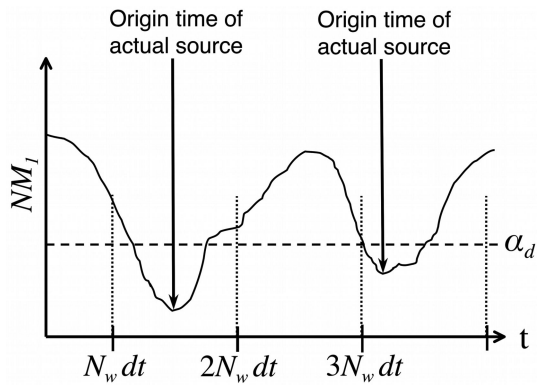
**Figure 3.** Idealized representation of the $NM_i$ variable along time. The parameter $\alpha_d$ is the detection threshold. In this example, the maximum number of iterations is set at $N_s = 1$. Note that in the limiting case $N_w = 1$, a seismic source would be declared at all time positions where $NM_1 < \alpha_d$ producing multiple spurious sources. On the other hand, if $N_w$ is for example four times bigger than it is showed, $N_s$ must have a minimum value of 2 to detect the two sources appearing as valleys in the $NM_1$ function.

computed using the updated residual $\mathbf{r}_i$, in other words

$$NM_i = \frac{||\mathbf{r}_i||_2^2}{||\mathbf{u}||_2^2}.$$

Then, if $NM_i > \alpha_d$ the algorithm stops iterating and restarts computations with a new observations vector. The seismic traces that form the new observations vector contain the last $N_G$ entries from the previous input traces plus $N_w$ newly recorded samples. In this way, the algorithm looks for seismic sources at all possible alignment positions allowed by the spatial and temporal sampling rates of the system (see example in Fig. 3). For multiple simultaneous sources where $N_s > 2$, the fitting of the solution with the observations is shared between the contributions from each source. In these cases, a detectability criteria requires a more elaborated approach. One possibility is to set a second parameter $\beta$ defining a minimum improvement in fitting required to declare a new source for all $i > 1$. The parameter $\alpha_d$ would still be the minimum fitting required to accept the whole solution. Multiple sources scenarios are not analysed in detail in this work. However, a synthetic example of multiple sources solved with the same fundamental ideas presented here can be consulted in Vera Rodriguez *et al.* (2010a). In the following section, the modified BOMP is tested in a synthetic scenario pertaining to the microseismic monitoring of a hydraulic fracture in an oil well, and with a real data set from the 2002 June 18 Caborn, Indiana, earthquake. In both cases, the computational work was performed using a desktop computer with processor speed of 2.93 GHz and 8 GB in direct access memory. The code has not yet been parallelized, hence, all the computations were performed using a single core of the computer.

## 4 APPLICATION TO SYNTHETIC AND REAL DATA EXAMPLES

### 4.1 Hydraulic fracturing in an oil well

Oil and gas wells are fractured through the injection of fluids at high pressures to enhance production (Cipolla & Wright 2002). Monitoring and processing of the microseismic activity generated during the injection process is a tool to study the properties of the induced fractures (Maxwell 2005; Warpinski 2009). For such objective, arrays of recording stations are positioned either on the surface or
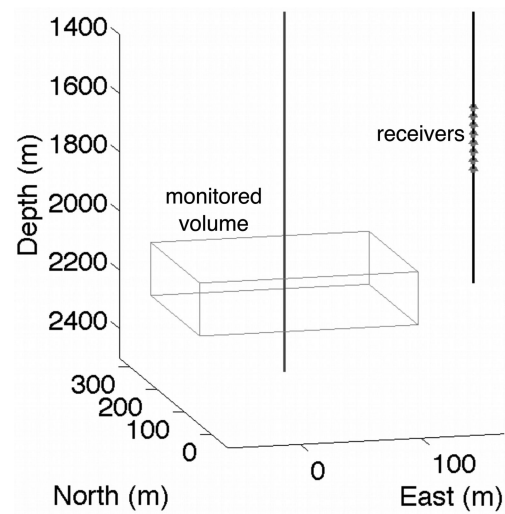


**Figure 4.** Geometry of the microseismic monitoring experiment used to test the modified BOMP. The treatment well passes through the monitored volume, which is outlined by a grey box. The monitoring well is where the receiver locations are displayed.

inside nearby wells (Duncan & Eisner 2010; Maxwell *et al.* 2010). In this synthetic example, we consider the case of recording stations positioned downhole. In the following, the well subject to hydraulic fracturing will be referred to as the treatment well, while the well where the recording stations are positioned will be called the monitoring well. Both, treatment and monitoring wells in this example are vertical (Fig. 4). The injection point in the treatment well is located at a depth of 2000 m, which also corresponds to the centre of the grid where the algorithm will detect seismic events. Discretization of the subsurface using a grid introduces error in the estimated seismic locations. In a regular grid this error is at most $a\sqrt{3}/2$, where $a$ is the distance between nodes, constant in all coordinate directions. This maximum discretization error corresponds to a source with actual location at the centre of a grid cell, and whose estimated location can only be attributed to one of the nearby nodes. Although there is no restriction on the location of the nodes for the purpose of running the algorithm, the use of a regular grid simplifies the calculations. Three different combinations node distance–maximum frequency content are used in these experiments, they are: $a = 10$ m, $f_{max} = 100$ Hz (model 1), $a = 10$ m, $f_{max} = 400$ Hz (model 2) and $a = 40$ m, $f_{max} = 400$ Hz (model 3). The maximum errors due to spatial discretization in these three models are considered reasonable given the magnitude of location errors usually expected in a microseismic monitoring application (Eisner *et al.* 2009, 2010; Kidney *et al.* 2010). Furthermore, the maximum frequency content allowed in each model is also consistent with what could be expected for receivers located at the horizontal distances defined in these experiments (e.g. Shemeta & Anderson 2010). Additional simplifications in the design of the experiment are the use of a homogeneous isotropic (ISO) medium and a relatively small number of grid nodes ($N_x = N_y = N_z = 9$). The total number of nodes in the grid is $N_t = N_x \times N_y \times N_z = 729$, which depending on the distance between nodes, corresponds to an also different monitored volume. The monitoring well is located at a horizontal distance of 400 m in the N35°E direction. An array of eight receivers with equal separations of 30 m between them, spans a longitude of 210 m from 1700 to 1910 m of depth in the monitoring well (Fig. 4). All these parameters reflect realistic geometrical settings for actual monitoring applications (see e.g. Eisner *et al.* 2010). Green's

functions and synthetic sources are computed using ray tracing theory and correcting for the source radiation pattern (Aki & Richards 2009), all traces are compared as velocity seismograms, rotated to a vertical-transverse-radial system and low-pass filtered to the maximum frequency content referred in each model. Moment tensor inversions using a vertical array of receivers cannot resolve the dipole perpendicular to the plane formed by the source hypocentre and the receivers (Nolen-Hoeksema & Ruff 2001; Vavrycuk 2007), therefore, a deviatoric constraint is applied to all cases in these synthetic experiments.

### 4.1.1 Influence of noise content on the solutions

We gauge the effect of noise through the signal-to-noise ratio (SNR), which is defined as $\mathrm{SNR} = \max(|\mathbf{u}|)/\sigma_n$, where $\sigma_n$ is the standard deviation of $\mathbf{n}$, a zero mean gaussian noise vector, and $\max(|\mathbf{u}|)$ is the maximum absolute value of the amplitudes in the current observation vector. At each node of the grid, five random sources are modelled for a total of $5 \times N_t = 3645$ realizations in each of the three previously described models. Each set of realizations is then subjected to the required values of $\mathrm{SNR} = 0.1, 0.5$ and $1$. The average location error (ALE) for a given model-SNR combination is computed by

$$\mathrm{ALE} = \sum_{n=1}^{N_t} \left( \frac{\sum_{k=1}^{k_s} ||\boldsymbol{\xi}_n - \boldsymbol{\xi}_k||_2^2}{k_s} \right) \Big/ N_t, \tag{16}$$

where $k_s$ is the number of sources that the algorithm was able to resolve at node $n$ (i.e. $k_s \in [1, 5]$). $\boldsymbol{\xi}_n$ is the actual source (node) location and $\boldsymbol{\xi}_k$ is the source location estimation for the $k$th source. Similarly, the error in the moment tensors is estimated by an average

normalized mean squared error (ANMSE),

$$\mathrm{ANMSE} = \sum_{n=1}^{N_t} \left[ \left( \sum_{k=1}^{k_s} \frac{\|\mathbf{m}_n^k - \hat{\mathbf{m}}_n^k\|_2^2}{\|\mathbf{m}_n^k\|_2^2} \right) \Big/ k_s \right] \Big/ N_t, \tag{17}$$

where $\hat{\mathbf{m}}_n^k$ is the inversion output for the $k$th source at $n$ and $\mathbf{m}_n^k$ its actual value. In this calculation we only consider the five elements of the moment tensor that are constrained by the monitoring geometry (Jechumtalova & Eisner 2008). The average origin time error (AOTE) is computed from

$$\mathrm{AOTE} = \sum_{n=1}^{N_t} \left( \frac{\sum_{k=1}^{k_s} |\mathrm{OT}_n - \mathrm{OT}_k|}{k_s} \right) \Big/ N_t, \tag{18}$$

where $\mathrm{OT}_n$ and $\mathrm{OT}_k$ represent the groundtruth and estimated values for the $k$th source at node $n$, respectively. As expected, increasing the SNR would improve the accuracy of the results. For moderate SNR levels (e.g. $\mathrm{SNR} = 1$ and $0.5$, Fig. 5), the three models display low errors in all estimated source parameters. The higher errors and standard deviations for location and origin time estimates are observed in models 1 and 2 with 10 m separation between nodes (Figs 5b and c). Between these two models, model 1 with 100 Hz frequency content present slightly higher magnitude of errors and standard deviations. These results can be analysed in the context of the coherence between Green's functions. The lower the frequency content and smaller the distance between nodes, the Green's functions between different nodes in the grid are more alike, hence the modified BOMP has more trouble identifying the correct solution. In the case of the source parameters, the behaviour reverses (Fig. 5a), now it is model 3 which presents the higher magnitude of errors and standard deviations. This effect is in response to the higher separation between nodes (40 m) and frequency content (400 Hz) with respect to the other models. The higher overlapping of Green's functions in models 1 and 2 produces better estimates
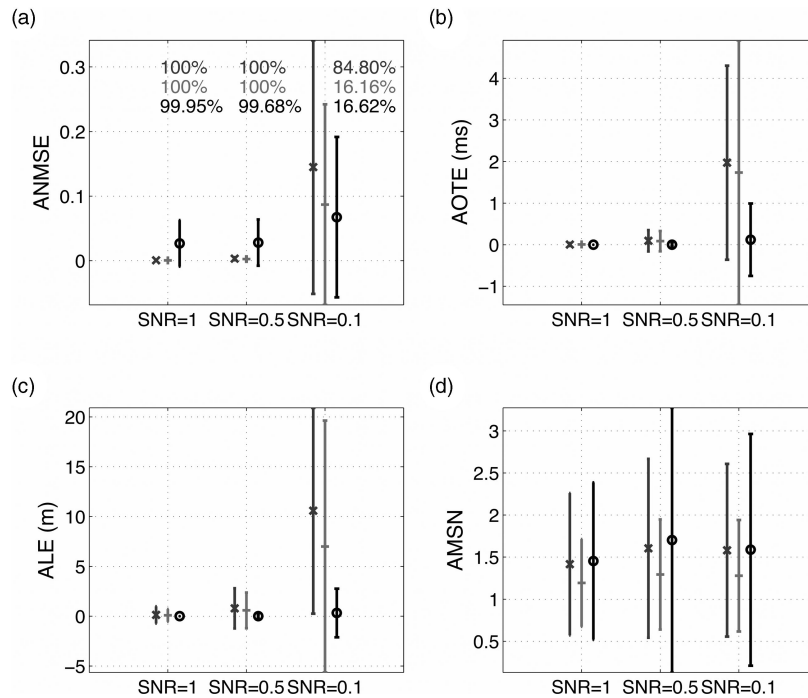


**Figure 5.** Average source parameter inversion errors for different levels of SNR. Crosses corresponds to model 1, dashes to model 2 and circles to model 3. (a) Error in moment tensor estimation, the percentages relate to the number of realizations resolved by the algorithm in each SNR level (top values correspond to model 1, followed by models 2 and 3), (b) error in origin time, (c) error in location and (d) average value of the index $p \in [1, n_h]$ where the solutions were found. Vertical bars are standard deviation.
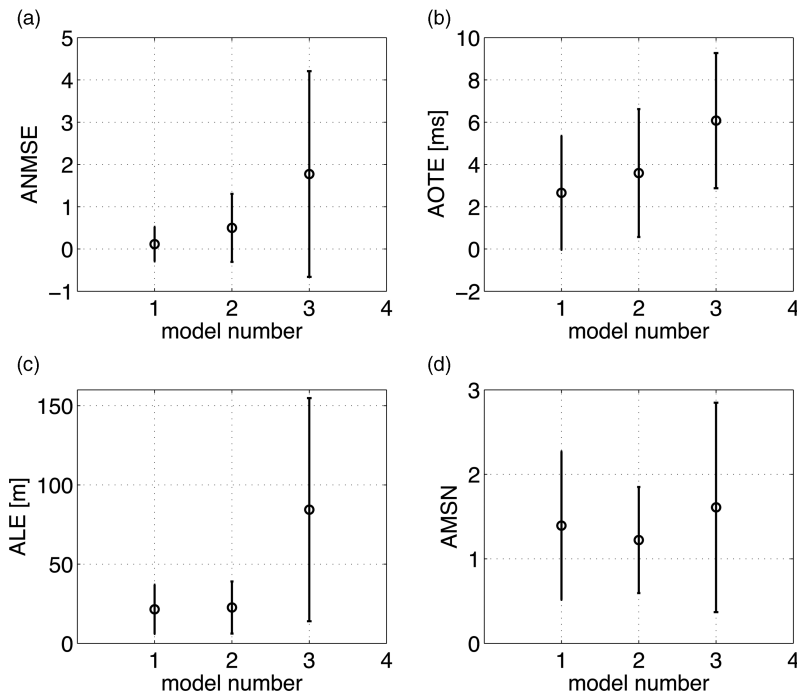
**Figure 6.** Effects of inaccurate Green's functions in the inversion output. The inaccuracy in the Green's functions is due to source locations not coinciding with the grid nodes. (a) Error in moment tensor estimation, (b) error in origin time, (c) error in location and (d) average value of the index $p \in [1, n_h]$ where the solutions were found. Vertical bars are standard deviation.

of moment tensors for slightly mislocated sources as compared to model 3 where the overlap is less. Additionally, this lack of overlapping increases the value of the NM in mislocated events, generating more missed sources in model 3 (see percentages in Fig. 5a). Hence, there is a trade-off in the amount of overlapping between the Green's functions, which on one hand helps to obtain more robust moment tensor estimates, but on the other, makes it harder for the modified BOMP to identify the optimum locations and origin times. In the presence of very low SNR (e.g. SNR = 0.1, Fig. 5), the algorithm has difficulties detecting the synthetic events (see percentages in Fig. 5a). The only case where a considerable amount of events is resolved is model 1. However, this effect is only a result of the high overlapping between the Green's functions in this model. In other words, since the Green's functions from multiple nearby nodes are highly coherent (alike), then, the solutions can have large errors in location and origin time and still produce a NM that will pass the detectability threshold. The less the overlap between Green's functions, the less the number of sources detected by the algorithm (with $n_h$ constant), however, the quality of the source parameters of the sources that are detected is improved. For sources that pass the detectability criteria, the number of the index $p \in [1, n_h]$ where the solutions are found remains stable in all the experiments (Fig. 5d). In general, a possibility to increase the number of detected sources is to increase the value of $n_h$, in this case, a trade-off exists with respect to the associated increase in processing time.

### 4.1.2 Influence of inaccurate Green's functions on the solutions

The effect of inaccurate Green's functions is examined using two examples. First, we compute Green's functions and a set of 400 observations vectors, both using the same velocity model. By design, the source location of these observations does not coincide with any of the grid nodes. In the second scenario, we introduce perturbations to the Green's function computations and adopt a set of 400 sources

that overlap with the grid node locations. For actual source locations that do not coincide with the grid nodes, the errors in the estimated source parameters increase as the overlap between Green's functions of different nodes is reduced (Figs 6a–c). The effect is similar for inaccurate Green's functions that result from an inexact velocity model (Figs 7a–c). As one would expect, the more inexact the velocity model, the higher the errors in the estimated source parameters. Again, the number of the index $p \in [1, n_h]$ where the solutions are found remains stable in all cases (Figs 6d and 7d). These results suggest that a highly coherent dictionary provides estimations that are more robust to errors introduced by inaccuracies of the dictionary itself. On the other hand, highly coherent dictionaries present a difficulty for the modified BOMP to find optimum solutions. Increasing the variable $n_h$ would help the algorithm, however, this would be at the expense of increasing computing time. A practical way to design a dictionary of Green's functions for a real application is through numerical experiments like the ones just presented. Following the results from our experiments, model 2 with distance between nodes of 10 m and maximum frequency content of 400 Hz seems to provide a good trade-off between detectability and errors expected in the solutions. Furthermore, these properties can also be improved by setting the variable $n_h$ at a level that is reasonable in terms of the required speed at which solutions have to be output.

### 4.2 Application to the 2002 June 18 Caborn, Indiana, earthquake

The 2002 June 18 Caborn, Indiana, earthquake is a moderate-sized earthquake with a well-studied source location and seismic moment tensor. The event occurred in the Wabash Valley Seismic Zone (WVSZ), located in the central eastern United States shared by the states of Indiana, Illinois and Kentucky (Langer & Bollinger 1991, Fig. 8). Considering its seismic activity, the Wabash Valley
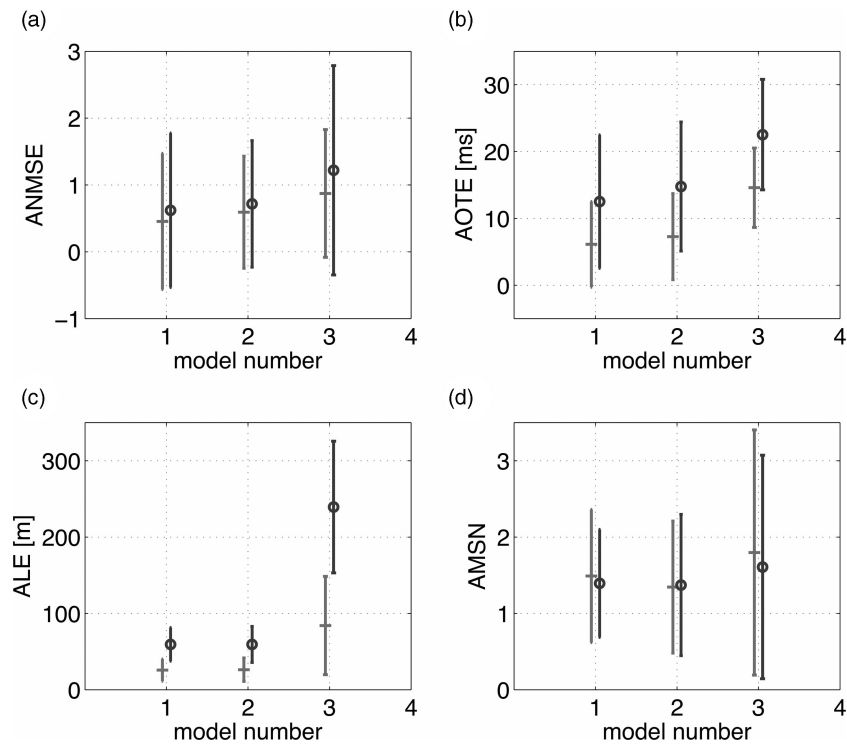
**Figure 7.** Effects of inaccurate Green's functions in the inversion output. After computing the observations, the velocity model is perturbed by 5 per cent (circles) and 3 per cent (dashes) to compute dictionaries of Green's functions. (a) Error in moment tensor estimation, (b) error in origin time, (c) error in location and (d) average value of the index $p \in [1, n_h]$ where the solutions were found. Vertical bars are standard deviation.
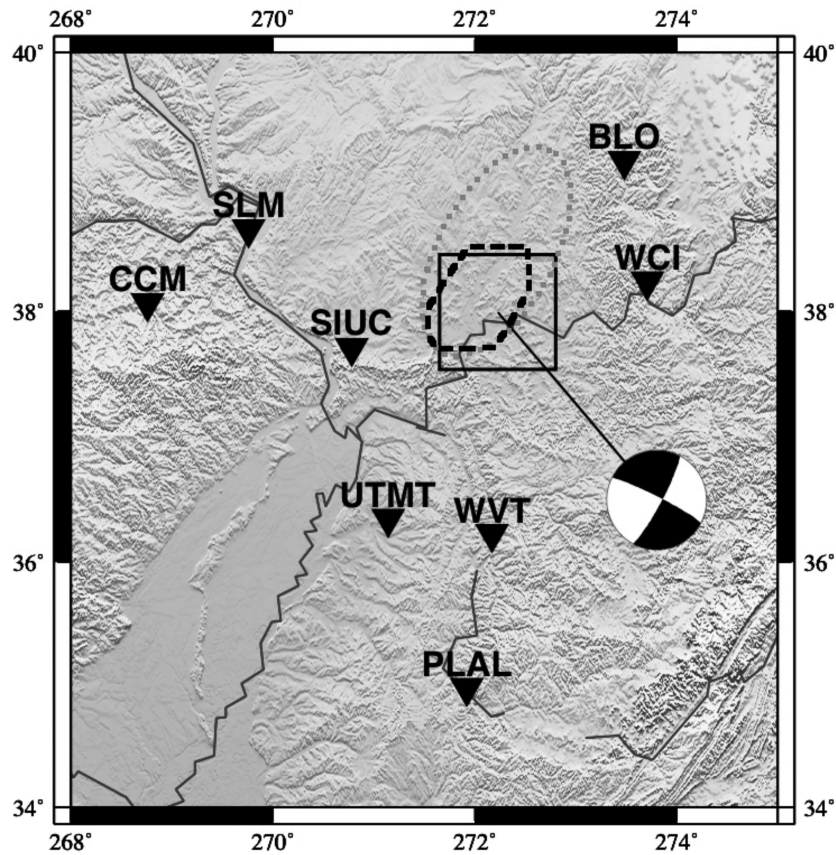


**Figure 8.** Epicentral location of the 2002 June 18 Caborn, Indiana, earthquake and distribution of seismic stations considered in this work (black triangles). The beach ball corresponds to the solution obtained by Kim (2003). The Wabash Valley Seismic Zone (WVZS) is delimited by the dotted line. The Wabash Valley Fault System (WVFS) is enclosed by the dashed line. The black square is the surface projection of the grid used in this work.
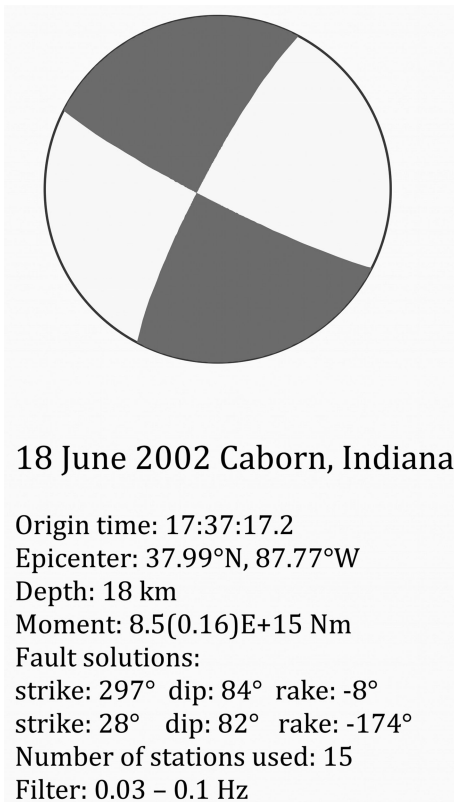
## 18 June 2002 Caborn, Indiana

Origin time: 17:37:17.2
Epicenter: 37.99°N, 87.77°W
Depth: 18 km
Moment: 8.5(0.16)E+15 Nm
Fault solutions:
strike: 297°  dip: 84°  rake: -8°
strike: 28°   dip: 82°  rake: -174°
Number of stations used: 15
Filter: 0.03 – 0.1 Hz

**Figure 9.** Source parameters of the 2002 June 18 Caborn, Indiana, earthquake determined by Kim (2003). The source mechanism is represented by the beach-ball diagram (lower hemisphere projection).

is a prominent region of Illinois, since it is the only part that does not behave as an intraplate region (Kontar *et al.* 2010). A focus of seismic activity in the WVSZ is the Wabash Valley Fault System (WVFS), which is a system of subsurface normal faults that run parallel to the Wabash River Valley. The faults are high angle, trending north–northeast and have been mapped down to more than 7 km penetrating the Precambrian basement (Bear *et al.* 1997). The WVFS covers an approximate area of 90 × 50 km (see Fig. 8), the faults have been interpreted to split upwards outlining horsts and grabens (Nelson 1991). Kim (2003) infers that the WVFS could have initiated during the Iapetean, while the region was rifting, however Kontar *et al.* (2010) point out that timing and origin of the deep faults remain unknown. Based on an analysis that includes the 2002 June 18 earthquake, Kim (2003) suggests the reactivation of a possible Precambrian rift system by the contemporary regional stresses. A description of the source parameters of the 2002 June 18 event determined by Kim (2003) is presented in Fig. 9. These results were obtained from the use of a 1-D velocity model (Table 1) and the recordings from 15 seismic stations with epicentral distances in the range 129–585 km. The epicentral location, source mechanism and

depth of the event were determined separately. The source mechanism and depth were estimated using a waveform fitting method that looks for the best DC solution within a grid spanning the (strike, dip and rake) space, and the best depth within a range of values (Zhao & Helmberger 1994). The depth of the event was further corroborated by analysing teleseismic *P* waves (∼19 km). The dominant phases in the filtered regional seismograms are fundamental Rayleigh and Love waves, although body waves (*P*) from the eight closest stations were also considered. The epicentral location was ultimately refined using *P*- and *S*-wave time picks from 20 local and regional seismic stations and the depth from the source mechanism inversion. To test our inversion algorithm, we formulate a hypothetical monitoring system around the WVFS to detect and invert for the source parameters of the 2002 June 18 event.

### 4.2.1 Description of the monitoring system

The hypothetical system consists of eight broad-band seismic stations in the approximate distance range of 100–300 km from WVFS (Fig. 8, Table 2). The monitored volume is divided using a grid of $21 \times 21 \times 5 = 2205$ nodes or virtual sources. The distance between the nodes is 5 km both in the horizontals X(North), Y(East) and depth directions. The surface projection of the grid covers an area of $100 \times 100$ km outlining practically all WVFS. The node depths range from 5.5 to 25.5 km, which also cover the maximum proposed depth of the seismogenic region (∼20 km). Following Kim (2003), the frequency range considered is 0.01–0.1 Hz. Similar combinations of distance between nodes and frequency content are used in the GridMT system (Tsuruoka *et al.* 2009), and for the study of earthquakes offshore Northern California (Guilhem & Dreger 2010). In these two latter works, the detection threshold is set using a variance reduction (VR) measurement defined as

$$VR = 100(1 - NM). \tag{19}$$

In the GridMT system the detection threshold is VR ≥ 65.0, solutions present VRs of similar magnitude in the offshore California system. Considering the relationship between the VR and the NM, the detection threshold in our system is set at $\alpha_d \leq 0.35$. For each set virtual source-recording stations, six Green's functions corresponding to each of the elemental force couples in the seismic moment tensor are computed and arranged in a dictionary. Both the Green's functions and observations are frequency filtered, rotated to a radial, transverse, vertical system and processed to be compared as velocity records. Furthermore, amplitudes are normalized, hence no scalar moment estimate is provided for this example. The Green's functions are computed using the velocity model displayed in Table 1 using the reflectivity method from Randall (1994). The duration of the Green's functions is 150 s, which considering a sampling rate

**Table 1.** Velocity model used in the Caborn, Indiana, earthquake inversion (Kim 2003).

| Depth (km) | $Vp$ (km s$^{-1}$) | $Vs$ (km s$^{-1}$) |
|---|---|---|
| 7 | 5.9 | 3.4 |
| 28 | 6.5 | 3.7 |
| | 8.0 | 4.5 |

**Table 2.** List of seismic stations used in the hypothetical monitoring system.

| Name | Lat (°) | Lon (°) | Elevation (km) |
|---|---|---|---|
| SIUC | 37.71 | −89.22 | 120 |
| WCI | 38.23 | −86.29 | 210 |
| BLO | 39.17 | −86.52 | 246 |
| UTMT | 36.35 | −88.86 | 110 |
| WVT | 36.13 | −87.83 | 153 |
| SLM | 38.64 | −90.24 | 186 |
| CCM | 38.06 | −91.24 | 222 |
| PLAL | 34.98 | −88.08 | 165 |

of $\Delta t = 1$ s is equivalent to 150 samples. The total response time ($t_R$) of the system is

$$t_R = t_{N_G} + t_{N_w} + t_T + t_p, \qquad (20)$$

where $t_{N_G} = 150$ s is the duration of the Green's functions, $t_{N_w}$ is the length of the processing window, $t_T$ is the transmission time from the recording stations to the computing centre and $t_p$ is the processing time of our algorithm. The duration of the observation vectors that input the inversion is $t_{N_u} = t_{N_G} + t_{N_w}$. A new vector of observations enter the inversion every $t_{N_w} + \Delta t$ seconds. Our objective is that $t_p \leq t_{N_w} + \Delta t$, in other words, the system must provide an answer before new information is available to be inverted. The inversion is set to look for a maximum of 1 source at each input observation vector (i.e. $N_s = 1$). The search for optimum solutions in the modified BOMP is set to $n_h = 200$.

### 4.2.2 Inversion of the 2002 June 18 earthquake records

To simulate the detection and inversion of the 2002 June 18 earthquake, the seismic recordings of the event are cut from 60 s before the origin time determined by Kim (2003) and up to 240 s after. The processing window is then set as $N_w = 30$ samples. Given the length of the Green's functions and the sampling rate, this means that a set of five observation vectors **u** will input the inversion process. The required processing time to guarantee a real-time response is $t_p \leq 31$ s. The average processing time observed during the tests was $\bar{t}_p \sim 4$ s, corroborating the feasibility of real-time monitoring using the hypothetical system, and furthermore that a bigger number of grid nodes and/or recording stations can be used. A disadvantage in the use of adjacent processing windows is the possibility to detect the same seismic event more than once when its origin time is close to the limit of the processing window. Alternatives to overcome this limitation are the use of overlapping windows and/or the comparison of results between different adjacent windows (e.g. Tsuruoka *et al.* 2009). To analyse with more detail the estimated source mechanism the inversion is run twice, once applying the deviatoric constraint and the other allowing a full moment tensor recovery. The percentages of ISO, DC and compensated linear vector dipole (CLVD) for each solution are presented in Table 3 (Knopoff & Randall 1970; Vavrycuk 2001). In the deviatoric solution, the percentage of ISO component is negligible, on the other hand, in both results the source mechanism is predominantly DC. The amount of CLVD percentage in both solutions is associated to the angle that the slip vector deviates from the fault plane ($\alpha$). The small magnitude of $\alpha$ supports agreement between our results and the assumption of pure DC mechanism used by Kim (2003). Furthermore, the existence of an $\alpha \neq 0$ might be in part due to the presence of noisy components in the input records. In its current version, our algorithm does not have a mechanism to filter out of the inversion traces with low SNR, which can introduce bias into the inversion results. The origin time and hypocentre location in both of our solutions is the same. Although the grid was designed

**Table 3.** Decomposition in percentages of isotropic (ISO), double couple (DC) and compensated linear vector dipole (CLVD) of source mechanism solutions for the 2002 June 18 Caborn earthquake. Negative percentages in ISO and CLVD components are associated to compressive faults, $\alpha$ is the angle formed between the fault plane and the slip vector (Vavrycuk 2001).

| Type of constraint | Per cent ISO | Per cent DC | Per cent CLVD | $\alpha$ (°) |
|---|---|---|---|---|
| No constraint | −4 | 67 | −29 | −14 |
| Deviatoric | 0 | 70 | −30 | −14 |

on purpose not to coincide with the hypocentre determined by Kim (2003), our algorithm determined the event location at the node that was closest to Kim's solution. Particularly, our results show the depth of the event at 20.5 km, which agrees better with the event's depth determined from teleseismic waves ($\sim$19 km). A summary of the solution using the deviatoric constraint is presented in Fig. 10.

### 4.3 Comparison with other real-time inversion methodologies

The introduction of this work presents a rough overview of source parameter inversion methods in earthquake seismology and microseismic monitoring in oil and gas wells. The list of available methodologies to invert for the source parameters is even longer if we consider other areas of applied geophysics, for example, mining applications (Gibowicz 2009). Although the methodology presented in this work has not been tested as extensively as the methodologies mentioned in the Introduction, it presents capabilities that are appealing for the development of new more powerful source parameter inversion techniques using the theory of sparse representations. As it was mentioned earlier, most source parameter inversion techniques require the calculation of origin time and location (either epicentre or hypocentre) before starting the estimation of the source mechanism, since this is usually performed by independent algorithms, a waiting time is implicitly required for the estimation of the moment tensor. The BOMP method proposed here overcomes this limitation, making it suitable for the continuous automatic real-time recovery of the three source parameters simultaneously. Another methodology that presents these capabilities is the grid search approach proposed by Kawakatsu (1998). Similar to BOMP, the grid search approach is input with a continuous flow of seismic recordings, it does not require *a priori* information about event occurrence, and the output from the systems are the three source parameters (origin time, hypocentre location and moment tensor). Additionally, in both cases the monitored volume is divided using a grid. It is also this parametrization of the subsurface into a grid that imposes the main limitations for both systems, which are related to the maximum number of grid nodes (virtual sources) and recording stations that can be inverted in real time. Kawakatsu's method is currently implemented in the ERI of Japan under the name GridMT (Tsuruoka *et al.* 2009). GridMT divides the subsurface using a grid and then solves the system in (12) at each grid node. The least-squares solution to (12) is $\mathbf{m}_n = (\mathbf{G}_n^T \mathbf{G}_n)^{-1} \mathbf{G}_n^T \mathbf{u}$, where $n$ is a node index. To reduce computational effort during the inversion, matrix $\mathbf{A}_n = (\mathbf{G}_n^T \mathbf{G}_n)^{-1}$ is computed for all the grid nodes and saved in memory. Hence, at each time step, matrix $\mathbf{A}_n$ is multiplied by the product $\mathbf{b}_n = \mathbf{G}_n^T \mathbf{u}$ between the observations $\mathbf{u}$ and the Green's functions from each node $\mathbf{G}_n$. Then, GridMT performs a grid search for the node with the solution $\mathbf{m}_n$ that gives the highest VR. From this description, two differences between BOMP and GridMT are immediately obvious. First, since matrix $\mathbf{A}_n$ is already computed in GridMT, it is not possible to alternate between deviatoric and full moment tensor solutions, unless two different versions of $\mathbf{A}_n$ are pre-computed and saved. In our method, the constraint for deviatoric solutions is easily switched on and off at step 3 (and 2.1 in the modified BOMP). Furthermore, in single source scenarios like earthquake monitoring, a non-linear pure DC constraint could also be incorporated in step 3 by replacing the least-squares source mechanism determination with an algorithm that performs a search over a (dip, rake and strike) solution space (e.g. Zhu & Helmberger 1996). The second difference is related to the comparison between Green's functions and
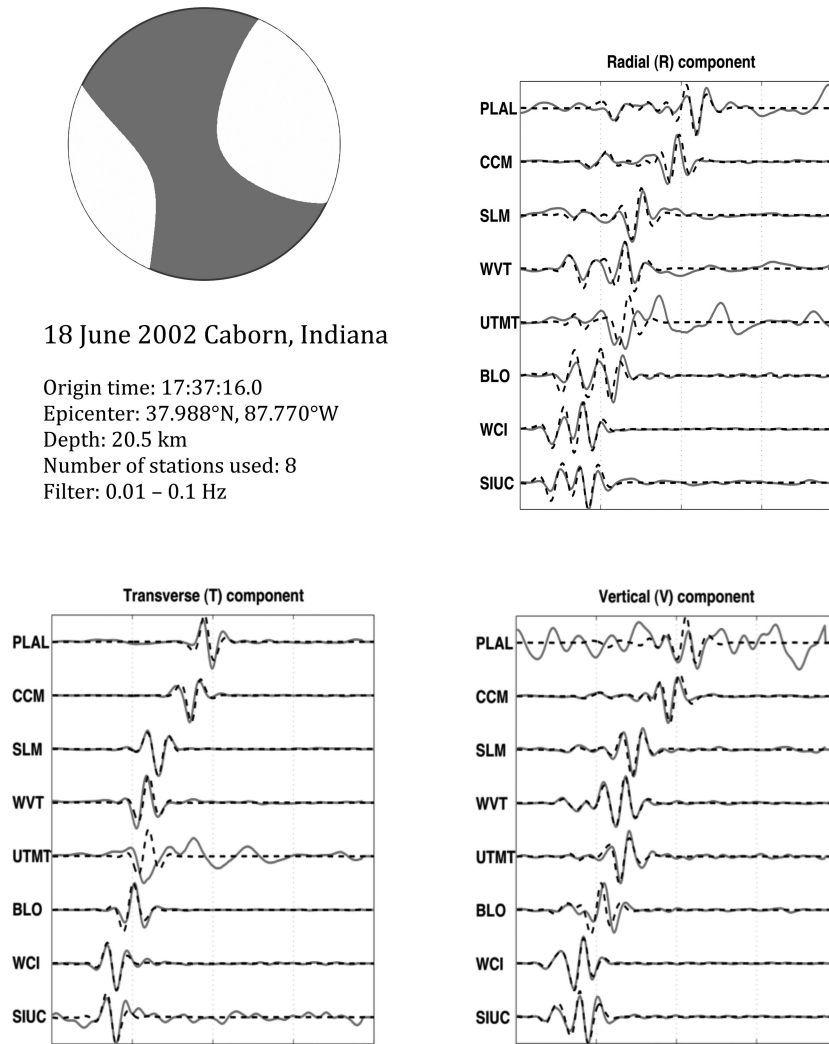
**18 June 2002 Caborn, Indiana**

Origin time: 17:37:16.0
Epicenter: 37.988°N, 87.770°W
Depth: 20.5 km
Number of stations used: 8
Filter: 0.01 – 0.1 Hz

**Figure 10.** Source parameters of the 2002 June 18 Caborn, Indiana, earthquake determined by our hypothetical monitoring system. The source mechanism is represented by the beach-ball diagram (lower hemisphere projection). Solid line: observed records. Dotted line: synthetic records obtained from the forward modelling of our solution.

observations. In both methodologies the product $\mathbf{b}_n$ is computed at each node (consider a single time step in both cases). This is the part of the process that takes the highest computational cost. In our method an extra step determines the $\ell_2$-norm of each $\mathbf{b}_n$. GridMT then calculates the product $\mathbf{A}_n\mathbf{b}_n$ for all nodes, while our method computes this product for only the $n_h$ nodes that present the highest $||\mathbf{b}_n||_2^2$ values, where $n_h$ is much smaller than the total number of nodes in the grid. This provides a subtle advantage in terms of computational speed to the modified BOMP. Additionally, an extra capability of BOMP-based methods is the possibility to identify more than one source contained in the same vector of observations $\mathbf{u}$.

## 5 DISCUSSION

Despite the differences mentioned, perhaps the most important relevance of the modified BOMP is that being based on sparse representation theory gives the possibility of using compressive sensing to push the limits of real-time applicability. Compressive sensing is a relatively new field of signal processing and applied mathematics that studies sampling and recovery conditions for signals that admit a sparse representation in a known basis or dictionary (Donoho

*et al.* 2006; Baraniuk 2007; Candes & Wakin 2008). Based on compressive sensing theory, Vera Rodriguez *et al.* (2010b) change the problem in (14) to the problem of solving

$$\mathbf{\Phi}u = \mathbf{\Phi}\mathbf{G}\mathbf{m}, \tag{21}$$

where $\mathbf{\Phi}$ is called a sensing matrix. The result of multiplying both sides of eq. (14) by the sensing matrix $\mathbf{\Phi}$ is a dimensionality reduction of the system of equations. It is this dimensionality reduction that allows a significant decrease in processing time and for instance, the use of a larger number of grid nodes, and also a considerably larger number of input records to the inversion without compromising the real-time response. A detailed description on the implementation of compressive sensing with our inversion method is the subject of ongoing research.

## 6 CONCLUSIONS

Through a convenient parametrization of the seismic source forward problem, we showed that the source mechanism is a sparse representation of the source displacement field under a dictionary of Green's functions. Hence, sparse representation theory provides alternative strategies for simultaneously inverting for the origin

time, hypocentre location and seismic moment tensor of seismic events. The modified BOMP is suitable to enforce block sparsity in the solutions and to identify optimal source parameters in the presence of highly coherent dictionaries. The BOMP method used in this work follows essentially the same workflow of the regular BOMP algorithm. The main difference comes from the physical meaning of the superdictionary used in the source parameter inversion, where solutions are found after matching the input observations both in 3-D space and time. Although, without giving consideration to its physical meaning, the superdictionary $\mathbb{G}$ could be treated as a regular dictionary, the high coherence between its columns makes difficult the identification of optimal solutions using the regular BOMP method. Hence, a modification based on a search over the largest values of the $\ell_2$-norm of the correlation between the blocks of the dictionary and the current residuals makes the algorithm more suitable to work in highly coherent dictionaries such as those that arise in seismic monitoring applications. Although the BOMP method has not been tested as extensively as other methodologies currently in use in different areas of geophysics, it presents capabilities that are of great interest for the development of improved source parameter inversion systems. One characteristic that differentiates BOMP from most other source inversion approaches is that it is specifically designed to be implemented as a continuous monitoring system. Also, it can potentially solve for multiple sources in the same set of observations that input the inversion. The most important consequence of using sparse representation theory is the possibility to integrate our method with compressive sensing. Using compressive sensing the limits for real-time implementation of the modified BOMP can be pushed further than those of other available real-time monitoring systems. This brings the possibility to monitor larger subsurface volumes with denser networks of recording stations.

## ACKNOWLEDGMENTS

## REFERENCES

Aki, K. & Richards, P., 2009. *Quantitative Seismology,* University Science Books, Sausalito, CA.

Baraniuk, R., 2007. Compressive sensing, *IEEE Signal Process. Mag.,* **24,** 118–121.

Bayuk, I., Ammerman, M. & Chesnokov, E., 2009. Estimation of shale's permeability from microseismicity, *SEG Expanded Abstracts,* **28,** 1581–1585.

Bear, G., Rupp, J. & Rudman, A., 1997. Seismic interpretation of the deep structure of the Wabash valley fault system, *Seism. Res. Lett.,* **68,** 624–640.

Bernardi, F., Braunmiller, J., Kradolfer, U. & Giardini, D., 2004. Automatic regional moment tensor inversion in the European-Mediterranean region, *Geophys. J. Int.,* **157**(2), 703–716.

Candes, E. & Wakin, M., 2008. An introduction to compressive sampling, *IEEE Signal Process. Mag.,* **25,** 21–30.

Chen, S., Donoho, D. & Saunders, M., 1998. Atomic decomposition by basis pursuit, *SIAM J. Sci. Comput.,* **20,** 33–61.

Cipolla, C. & Wright, C., 2002. Diagnostic techniques to understand hydraulic fracturing: what? why? and how?, in *SPE/CERI Gas Technology Symposium,* Calgary, Alberta, pp. 23–35.

Clinton, J., Hauksson, E. & Solanki, K., 2006. An evaluation of the scsn moment tensor solutions: robustness of the $m_W$ magnitude scale, style of faulting and automation of the method, *Bull. seism. Soc. Am,* **96,** 1689–1705.

Donoho, D., Elad, M. & Temlyakov, V., 2006. Stable recovery of sparse overcomplete representations in the presence of noise, *IEEE Trans. Inf. Theory,* **52,** 6–17.

Dreger, D.S., 2003. TDMT_INV: Time Domain Seismic Moment Tensor INversion, in *International Handbook of Earthquake and Engineering Seismology,* International Geophysics, Vol. 81B, pp. 1627–1627, eds, Lee, W.H.K., Kanamori, H., Jennings, P. & Kisslinger, C., Academic Press, San Diego, CA.

Dreger, D. & Helmberger, D., 1993. Determination of source parameters at regional distances with single station or sparse network data, *J. geophys. Res.,* **98,** 8107–8125.

Duncan, P. & Eisner, L., 2010. Reservoir characterization using surface microseismic monitoring, *Geophysics,* **75,** 75A139–75A146.

Dziewonski, A., Chou, T. & Woodhouse, J., 1981. Determination of earthquake source parameters from waveform data for studies of global and regional seismicity, *J. geophys. Res.,* **86,** 2825–2852.

Eisner, L., Duncan, P., Werner, H. & Keller, W., 2009. Uncertainties in passive seismic monitoring, *Leading Edge,* **28,** 648–655.

Eisner, L., Hulsey, B., Duncan, P., Jurick, D., Werner, H. & Keller, W., 2010. Comparison of surface and borehole locations of induced seismicity, *Geophys. Prospect.,* **58,** 809–820.

Eldar, Y.C. & Bolcskei, H., 2009. Block-sparsity: Coherence and efficient recovery, in *Proceedings of IEEE International Conference on Acoustics, Speech, and Signal Processing,* pp. 2885–2888, IEEE Computer Society, Los Alamitos, CA, USA.

Eldar, Y.C., Kuppinger, P. & Bolcskei, H., 2010. Block-sparse signals: uncertainty relations and efficient recovery, *IEEE Trans. Signal Process.,* **58**(6), 3042–3054.

Fischer, T., Hainzl, S., Eisner, L., Shapiro, S. & LeCalvez, J., 2008. Microseismic signatures of hydraulic fracture growth in sediment formations: observations and modeling, *J. geophys. Res.,* **113,** B02307, doi:10.1029/2007JB005070.

Gibowicz, S.J., 2009. Seismicity induced by mining: recent research, in *Advances in Geophysics,* Vol. 51, pp. 1–53, ed. Dmowska, R., Elsevier, Amsterdam.

Godano, M., Gaucher, E., Bardainne, T., Regnier, M., Deschamps, A. & Valette, M., 2010. Assessment of focal mechanisms of microseismic events computed from two three-component receivers: application to the Arkema-Vauvert field (France), *Geophys. Prospect.,* **58,** 775–790.

Guilhem, A. & Dreger, D., 2010. *Towards a Real-Time Earthquake Source Determination and Tsunami Early Warning in Northern California,* Tech. Rep., Berkeley Seismological Laboratory, UC Berkeley, Berkeley, CA.

Herman, M. & Strohmer, T., 2010. General deviants: an analysis of perturbations in compressed sensing, *IEEE J. Selected Topics Signal Process.,* **4,** 342–349.

House, L., Flores, R. & Whiters, R., 1996. Microearthquakes induced by a hydraulic injection in sedimentary rock, East Texas, *SEG Expanded Abstracts,* **15,** 110–113.

Jechumtalova, Z. & Eisner, L., 2008. Seismic source mechanism inversion from a linear array of receivers reveals non-double-couple seismic events induced by hydraulic fracturing in sedimentary formation, *Tectonophysics,* **460,** 124–133.

Kawakatsu, H., 1995. Automated near-realtime CMT inversions, *Geophys. Res. Lett.,* **94,** 2569–2572.

Kawakatsu, H., 1998. On the realtime monitoring of the long-period seismic wavefield, *Bull. Earthq. Res. Inst.,* **73,** 267–274.

Kidney, R., Zimmer, U. & Boroumand, N., 2010. Impact of distance-dependent location dispersion error on interpretation of microseismic event distributions, *Leading Edge,* **29,** 284–289.

Kim, W., 2003. The 18 June 2002 Caborn, Indiana, earthquake: reactivation of ancient rift in the Wabash valley seismic zone?, *Bull. seism. Soc. Am.,* **93,** 2201–2211.

Knopoff, L. & Randall, M., 1970. The compensated linear-vector dipole: a possible mechanism for deep earthquakes, *J. geophys. Res.,* **75,** 4957–4963.

Kontar, Y. *et al.*, 2010. Is the Wabash valley seismic zone related with the ancient reelfoot rift? in *GeoPRISMS Implementation Workshop: Rift Initiation and Evolution*, http://www.nsf-margins.org/RIE/2010/index.html.

Kowalski, M. & Torrésani, B., 2009. Sparsity and persistence: mixed norms provide simple signal models with dependent coefficients, *Signal Image Video Process.,* **3**(3), 251–264.

Langer, C. & Bollinger, G., 1991. The southeastern Illinois earthquake of 10 June 1987: the later aftershocks, *Bull seism. Soc. Am.,* **81,** 423–445.

Le Calvez, J., Tanner, K., Glenn, S., Kaufman, P., Sarver, D., Bennett, L., Panse, R. & Palacio, J., 2006. Using induced microseismicity to monitor hydraulic fracture treatment: a tool to improve completion techniques and reservoir management, in *Proceedings of SPE Eastern Regional Meeting,* Canton, OH, SPE104570.

LeCampion, B. & Jeffrey, R., 2004. Real-time estimation of fracture volume and hydraulic fracture treatment efficiency, in *Proceedings of North America Rock Mechanics Symposium: Rock Mechanics Across Borders and Disciplines,* Houston, TX, ARMA/NARMS04–519.

Lee, S., Huang, B., Liang, W. & Chen, K., 2010. Grid-based moment tensor inversion technique by using 3-d Green's functions database: a demonstration of the 23 October Taipei earthquake, *Terr. Atmos. Ocean. Sci.,* **21,** 503–514.

Madariaga, R., 2007. Seismic source theory, in *Treatise on Geophysics,* pp. 59–82, ed. Schubert, G., Elsevier, Amsterdam.

Mallat, S., 2008. *A Wavelet Tour of Signal Processing: The Sparse Way,* 3rd edn, Academic Press, Burlington, MA.

Mallat, S. & Zhang, Z., 1993. Matching pursuits with time-frequency dictionaries, *IEEE Trans. Signal Process.,* **41,** 3397–3415.

Maxwell, S., 2005. A brief guide to passive seismic monitoring, in *Proceedings of CSEG National Convention,* Calgary, Alberta, pp. 177–178.

Maxwell, S., Urbancic, T., Steinsberger, N. & Zinno, R., 2002. Microseismic imaging of hydraulic fracture complexity in the barnett shale, in *Proceedings of SPE Annual Technical Conference and Exhibition,* San Antonio, TX, SPE77440.

Maxwell, S., Rutledge, J., Jones, R. & Fehler, M., 2010. Petroleum reservoir characterization using downhole microseismic monitoring, *Geophysics,* **75,** 75A129–75A137.

Nelson, J., 1991. Structural styles of the Illinois basin, in *Interior Cratonic Basins,* pp. 209–243, eds Leighton, M., Kolata, D., Oltz, D. & Eidel, J., American Association of Petroleum Geologists, Tulsa, OK.

Nolen-Hoeksema, R. & Ruff, L., 2001. Moment tensor inversion of microseisms from the b-sand propped hydrofracture, m-site, Colorado, *Tectonophysics,* **336,** 163–181.

Pasyanos, M., Dreger, D. & Romanowicz, B., 1996. Toward real-time estimation of regional moment tensors, *Bull. seism. Soc. Am.,* **86,** 1255–1269.

Pati, Y., Rezaiifar, R. & Krishnaprasad, P., 1993. Orthogonal matching pursuit: recursive function approximation with applications to wavelet decomposition, in *Proceedings of the 27th Annual Asilomar Conference in Signals, Systems and Computers*, Pacific Grove, CA.

Randall, G., 1994. Efficient calculation of complete differential seismograms for laterally homogeneous earth models, *Geophys. J. Int.,* **118,** 245–254.

Romanowicz, B., 1982. Moment tensor inversion of long period Rayleigh waves: a new approach, *J. geophys. Res.,* **87,** 5395–5407.

Romanowicz, B., Dreger, D., Pasyanos, M. & Uhrhammer, R., 1993. Monitoring of strain release in central and northern California using broadband data, *Geophys. Res. Lett.,* **20,** 1643–1646.

Rothert, E. & Shapiro, A., 2007. Statistics of fracture strength and fluid-induced microseismicity, *J. geophys. Res.,* **112,** B04309, doi:10.1029/2005JB003959.

Rutledge, J. & Phillips, W., 2003. Hydraulic simulation of natural fractures as revealed by induced microearthquakes, Carthage Cotton Valley gas field, East Texas, *Geophysics,* **68,** 441–452.

Scognamiglio, L., Tinti, E. & Michelini, A., 2009. Real-time determination of seismic moment tensor for the Italian region, *Bull. seism. Soc. Am.,* **99,** 2223–2242.

Shapiro, S., Audigane, P. & Royer, J., 1999. Large-scale in situ permeability tensor of rocks from induced microseismicity, *Geophys. J. Int.,* **137,** 207–213.

Shemeta, J. & Anderson, P., 2010. It's a matter of size: magnitude and moment estimates for microseismic data, *Leading Edge,* **29,** 296–302.

Sileny, J., Hill, D., Eisner, L. & Cornet, F., 2009. Non-double-couple mechanisms of microearthquakes induced by hydraulic fracturing, *J. geophys. Res.,* **114,** B08307, doi:10.1029/2008JB005987.

Sipkin, S.A., 1982. Estimation of earthquake source parameters by the inversion of waveform data: synthetic waveforms, *Phys. Earth planet. Inter.,* **30**(2-3), 242–259.

Strang, G., 2006. *Linear Algebra and its Applications,* Thomson Brooks/Cole, Toronto.

Tajima, F., Megnin, C., Dreger, D. & Romanowicz, B., 2002. Feasibility of real-time broadband waveform inversion for simultaneous moment tensor and centroid location determination, *Bull. seism. Soc. Am.,* **92,** 739–750.

Tropp, J., 2004. Greed is good: algorithmic results for sparse approximation, *IEEE Trans. Inf. Theory,* **50,** 2231–2242.

Tsuruoka, H., Kawakatsu, H. & Urabe, T., 2009. Grid mt (grid-based real-time determination of moment tensors) monitoring the long-period seismic wavefield, *Phys. Earth planet. Inter.,* **175,** 8–16.

Vavrycuk, V., 2001. Inversion for parameters of tensile earthquakes, *J. geophys. Res.,* **106,** 16 339–16 355.

Vavrycuk, V., 2007. On the retrieval of moment tensors from borehole data, *Geophys. Prospect.,* **55,** 381–391.

Vera Rodriguez, I., Sacchi, M. & Gu, Y., 2010a. Continuous hypocenter and source mechanism inversion via a Green's function-based matching pursuit algorithm, *Leading Edge,* **29,** 334–337.

Vera Rodriguez, I., Sacchi, M. & Gu, Y., 2010b. Toward a near real-time system for event hypocenter and source mechanism recovery via compressive sensing, *SEG Expanded Abstracts,* **29,** 2140–2145.

Warpinski, N., 1994. Interpretation of hydraulic fracture mapping experiments, in *Proceedings of SPE Centennial Petroleum Engineering Symposium,* Tulsa, OK, SPE27985.

Warpinski, N., 2009. Integrating microseismic monitoring with well completions, reservoir behavior, and rock mechanics, in *Proceedings of SPE Tight Gas Completions Conference,* San Antonio, TX, SPE125239.

Warpinski, N., Wolhart, S. & Wright, C., 2001. Analysis and prediction of microseismicity induced by hydraulic fracturing, in *Proceedings of SPE Annual Technical Conference and Exhibition,* New Orleans, LA, SPE71649.

Zhao, L. & Helmberger, D., 1994. Source estimation from broadband regional seismograms, *Bull. seism. Soc. Am.,* **84,** 91–104.

Zhu, L. & Helmberger, D.V., 1996. Advancement in source estimation techniques using broadband regional seismograms, *Bull. seism. Soc. Am.,* **86**(5), 1634–1641.